Hindawi
Journal of Nanomaterials
Volume 2022, Article ID 7120982, 11 pages
https://doi.org/10.1155/2022/7120982

Research Article

Rheological Model for Generalized Energy and Mass Transfer through Hybrid Nanofluid Flow Comprised of Magnetized Cobalt Ferrite Nanoparticles

Fahad S. Al-Mubaddel,[1,2] F. M. Allehiany,[3] Taher A. Nofal,[4] Mohammad Mahtab Alam,[5] Aatif Ali,[6] and Joshua Kiddy K. Asamoah[7]

[1]*Department of Chemical Engineering, College of Engineering, King Saud University, Riyadh 11421, Saudi Arabia*
[2]*King Abdullah City for Renewable and Atomic Energy: Energy Research and Innovation Center, (ERIC), Riyadh 11451, Saudi Arabia*
[3]*Department of Mathematical Sciences, College of Applied Sciences, Umm Al-Qura University, P.O. Box 715, Makkah 21955, Saudi Arabia*
[4]*Department of Mathematics and Statistics, College of Science, Taif University, P.O. Box 11099, Taif 21944, Saudi Arabia*
[5]*Department of Basic Medical Sciences, College of Applied Medical Science, King Khalid University, Abha 61421, Saudi Arabia*
[6]*Department of Mathematics, Abdul Wali Khan University Mardan, KP 23200, Pakistan*
[7]*Department of Mathematics, Kwame Nkrumah University of Science and Technology, Kumasi, Ghana*

Correspondence should be addressed to Joshua Kiddy K. Asamoah; topeljoshua@gmail.com

Received 12 January 2022; Revised 18 February 2022; Accepted 5 April 2022; Published 22 April 2022

Academic Editor: Taza Gul

The goal of the current research is to evaluate a 3D stagnation point flow of Darcy Forchheimer's hybrid nanofluid (NF) through a heated wavy flexible cylinder under the influence of slip conditions and varying thickness. A numerical model is developed for the purpose to magnify the energy and mass transmission rate and maximize the efficiency and performance of thermal energy conduction for a variety of commercial and biological purposes through methanol-based hybrid NF flow consisting of cobalt ferrite and copper nanoparticles. Due to their inclusive range of applications, copper and cobalt iron oxide nanoparticles are gaining a lot of attention in medical and technical research. The model has been articulated in the form of a set of PDEs, which are reduced by the resemblance substitutions to the system of ODEs. The obtained 1st-order differential equations are further processed by the computational strategy PCM. For the sake of accuracy and credibility, the values are verified with the bvp4c package. The findings are physically exhibited and analyzed. It has been observed that the induced magnetic field lessens with the upshot of the magnetic term and enhances under the action of magnetic Prandtl number M. The energy profile declines due to the variation of thermal jump constraint and boosts with the absorption and generation term.

1. Introduction

The flow around convex and concave bodies have been studied extensively in order to ensure the safety of the buildings by minimizing vortex-flaking, which causes a substantial amount of drag, noise, and vibration. Shape alteration is used as a flow control strategy as geometric interruptions [1]. Flow within a circular cylinder is used in many engineering mechanisms, but far less study has been conducted on flow over a cylinder in a constrained domain, such as flow in a horizontal channel or pipe flow. Many circumstances, such as blood flow via surgical supplies in veins and flow through cylindrical items near walls, necessitate consideration of wall effects while scaling a problem. Furthermore, whereas unstructured and random forms of external roughness, such as those seen in nature, have been studied, other types of organized roughness have not. A 3D printed solid with regular sinusoidal ridges may take curliness on its

exterior [2]. When heat generation is created, Salahuddin et al. [3] investigated the differently designed nanomaterials that influenced the thermodynamic effectiveness and flow performance of nanoliquid flow owing to rigid and sinusoidal barriers. To assess the aerodynamic workloads of a 5 : 1 rectangular sinusoidal radius cylinder, Wu et al. [4] used a wind tunnel with numerous active mechanisms. Changing the amplitude and frequency results in a streamwise sequence that is completely coherent, Bilal et al. [5] investigated a nonuniform Maxwell nanoliquid flow across a stretched cylinder accompanied by a nonfluctuating suction/injection. It has been shown that the angular momentum of mass propagation grows considerably when the thermophoresis ratio is increased, but radial and angular velocity declines as the viscosity element is improved. Seo et al. [6] demonstrated a numerical estimation of a 3D flow through a rectangular enclosure. In comparison to a circular cylinder, the sinusoidal cylinder was tested to see if it might enhance total heat conduction efficiency. The influence of the cylinder shape on heat transition was noticeable, with performance improving by up to 27%. Bilal et al. [7] use up an angled extendable tube to explore the iron oxide Fe_3O_4 and carbon nanotube (CNT) hybrid nanofluid (HNF). The conclusions reveal that hybrid NF is the best heat enhancer and may be used for both heat transmission and cooling purposes. Some further applications, uses, and flow models can be found in [8–10].

In comparison to common fluids like gasoline, freshwater, solo nanoparticle nanofluids, and acetylene, HNF is a revolutionary type of fluid that excels at energy conversions. HNFs can be used for a variety of thermal applications, as well as freezing in high-heat environments [11]. Hybrid NFs are used in solar energy, heat pumps, heat converters, air conditioners, automobile industry, electrical coolers, generators, radioactive systems, transmitters, ships, and bioscience. In this work, we are focusing on copper (Cu) and cobalt ferrite ($CoFe_2O_4$) NPs in the universal solvent water. Copper NPs in plant water extracts may be generated using a "green" chemical method called electrodeposition. Copper nanoparticles are being used as carriers for new antitubercular drugs [12]. Copper acts as an antifungal, antibiotic, and antimicrobial agent when it is added to freshwater for coatings, polymers, and textiles. Dietary supplements containing copper have a high absorptivity. Copper alloys and metals have high tensile strength [13]. Cobalt (Co) and iron (Fe) are metals. Fe lowers interstitial resistance, allowing for charge/ion mobility on the surface and a considerable increase in specific capacitance [14]. The use of imaging techniques like MRI, PET, and CT scan, among others, has proved crucial in detecting diseases efficiently. MRI is the most versatile of them all since it can provide both functional and morphological information while keeping excellent image quality. To make it more functional, bimagnetic particles are used. Bimagnetic core-shell cobalt ferrite NPs have emerged as a feasible option for generating new MRI contrast agents with improved magnetization. Bimagnetic NPs may also be used for drug transport and photothermal treatment, making them suitable entrants for the progress of novel nanotheragnostic drugs. Magnetic hydrotherapy is used to treat tumors because cancer cells are more sensitive to tiny temperature variations than healthy tissue. As a result, a rise in local temperature generated by the accumulation of magnetic NPs can kill cancer cells in the tumor while having little effect on normal tissues [15].

Several mathematicians and researchers address the mathematical approach to the abovementioned applications and challenges. Bilal et al. [16], for example, looked at the effects of electric and magnetic forces on the flow of water-based ferrous oxides and carbon nanotubes hybrid NFs over two revolving surfaces. The electric factor boosts the momentum boundary layer while lowering the thermal factor. Ramesh et al. [17] performed the covalent bonding reaction and activation energy characteristics in the flow of HNF through a stream-wise location using $CoFe_2O_4$ and Fe3O4 in EG+water. Wang et al. [18] employed an MWCNT-Fe3O4 hybrid nanoliquid to model the effects of metallic foam and nanomaterial on a typical solid heat sink's thermal efficiency. Ibrahim et al. [19] assessed the effect of turbulators on enhancing energy efficiency, as well as the hydraulic efficiency of Cu water HNF in a solar accumulator, using numerical simulations and ANSYS software. The influence of concave and convex shape on the flow of a radiative hybrid NF (SiO2-MoS2/water) was investigated by Yaseen et al. [20]. The thermal efficiency boosts by 15.47 percent for flow over convex-shaped sheets and 14.28 percent for flow over beveled edge sheets when the volume percentage of SiO2 nanocrystals is raised from 1% to 5%. Wang et al. [21] experimentally and technically assessed the FeZn4Co/CNF electrocatalyst and discovered these nanomaterials. References [22–25] contain some relevant literature and applications of Cu and $CoFe_2O_4$ NPs in water for biomedical and engineering objectives.

Magnetization is among the most essential factors in manufacturing and engineering, with numerous uses. The interplay of fluid nanomaterials with magnetic fields affects the quality of various industrial items such as heat exchangers, gearboxes, and compressors. The impact of magnetic fields can regulate and make accessible the rate of cooling of numerous industrial devices. Magnetic fields are vital in interplanetary and astronomical magnetosphere applications, as well as aeronautic technologies and chemical science. The strength and distribution of the administered magnetics have a significant impact on the flow properties. Many academics submitted research articles in fluid mechanics that described the flow features under the influence of MHD. Hayat and Noreen [26] explored the role of thermal expansion and a generated MHD on the oscillatory transport of a 4th-order fluid across a vertical tunnel. Raju et al. [27] considered the cumulative implications of heat exchange and the exponential component on MHD flow across a semiplate. Some recent literature related to MHD hybrid nanofluid exists in [28–30].

The objective of this study is to build on a concept proposed by Salahuddin et al. [31] by investigating the effects of methanol-based hybrid NFs consisting of Cu and $CoFe_2O_4$ nanoparticles on heat and mass transmission. The fluid flow has been examined in a heated wavy flexible cylinder under the upshot of slip condition, variable thickness, Darcy

Forchheimer, heat absorption/generation, and chemical reaction. The second intention is to improve thermal energy conduction productivity and performance for a variety of commercial and biological applications. The PCM approach is used to simulate the problem, and the results are compared to those obtained using the Matlab software bvp4c.

2. Mathematical Formulation

We supposed the steady 3D stagnation point flow of HNF flow over a heated stretchy wavy cylinder. The hybrid NF is a solution of copper Cu and cobalt ferrite $CoFe_2O_4$ nanomaterial in methanol fluid. The cylinder is located on xy -surface where the fluid is considered at $z > 0$. We suppose that the cylinder radius is extreme at point A called the noddle point through which fluid flow passes. Along the y-axis the wavy side of the cylinder is fixed, where the z-axis and x-axis are normal and upright to the wavy cylinder surface. Functions $u_e = ax$ and $v_e = bx$ epitomize the component of velocity at the stagnation point A. Here a and b are constants, in such a way $|b| \le |a|, 0 < a$ (see Figure 1).

Furthermore, we are analyzing the comportment of hybrid NF flow under the act of persistent magnetic field partaking uniform strength M_0. We suppose that M_1, M_2, and M_3 are the magnetic field components in the directions of x, y, and z, respectively. At the cylinder surface, M_1 and M_2 approach to $M_e(x)$ and $M_e(y)$, where M_3 has vanished. Here, T_1 and T_w are the surface and wall temperatures of the cylinder. The fundamental calculations that regulate the fluid flow are defined as follows [31]:

$$\frac{\partial u}{\partial x} + \frac{\partial v}{\partial y} + \frac{\partial w}{\partial z} = 0, \tag{1}$$

$$\frac{\partial M_1}{\partial x} + \frac{\partial M_2}{\partial y} + \frac{\partial M_3}{\partial z} = 0, \tag{2}$$

$$u\frac{\partial u}{\partial x} + v\frac{\partial u}{\partial y} + w\frac{\partial u}{\partial z} - \frac{\mu_e}{4\pi\rho_{\text{hnf}}}\left(M_1\frac{\partial M_1}{\partial x} + M_2\frac{\partial M_1}{\partial y} + M_3\frac{\partial M_1}{\partial z}\right) = \rho_{\text{hnf}}\frac{\partial^2 u}{\partial z^2} + a^2 x - \frac{\mu_e}{4\pi\rho_{\text{hnf}}} M_e(x)\frac{dM_e(x)}{dx} - \frac{\nu}{k^*}u - Fu^2, \tag{3}$$

$$u\frac{\partial v}{\partial x} + v\frac{\partial v}{\partial y} + w\frac{\partial v}{\partial z} - \frac{\mu_e}{4\pi\rho_{\text{hnf}}}\left(M_1\frac{\partial M_2}{\partial x} + M_2\frac{\partial M_2}{\partial y} + M_3\frac{\partial M_2}{\partial z}\right) = \rho_{\text{hnf}}\frac{\partial^2 v}{\partial z^2} + b^2 y - \frac{\mu_e}{4\pi\rho_{\text{hnf}}} M_e(y)\frac{dM_e(y)}{dx} - \frac{\nu}{k^*}v - Fv^2, \tag{4}$$

$$u\frac{\partial M_1}{\partial x} + v\frac{\partial M_1}{\partial y} + w\frac{\partial M_1}{\partial z} - \left(M_1\frac{\partial u}{\partial x} + M_2\frac{\partial u}{\partial y} + M_3\frac{\partial u}{\partial z}\right) = \eta_0\frac{\partial^2 M_1}{\partial z^2}, \tag{5}$$

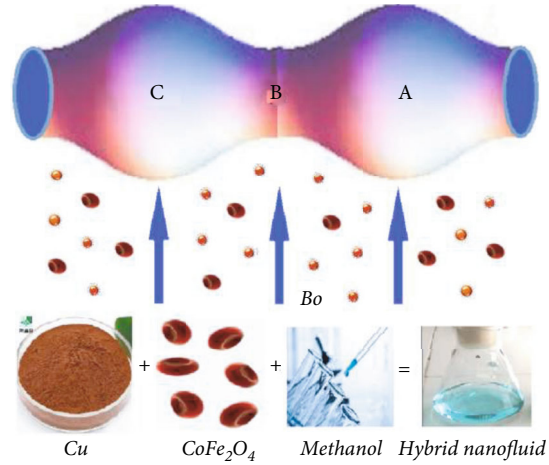

Figure 1: The hybrid nanofluid flows in a wavy heat cylinder.

$$u\frac{\partial M_2}{\partial x} + v\frac{\partial M_2}{\partial y} + w\frac{\partial M_2}{\partial z} - \left(M_1\frac{\partial v}{\partial x} + M_2\frac{\partial v}{\partial y} + M_3\frac{\partial v}{\partial z}\right) = \eta_0\frac{\partial^2 M_2}{\partial z^2}, \tag{6}$$

$$\left(u\frac{\partial T}{\partial x} + v\frac{\partial T}{\partial y} + w\frac{\partial T}{\partial z}\right) = \alpha_{\text{hnf}}\left(\frac{\partial^2 T}{\partial z^2}\right) + \frac{Q_0(T - T_\infty)}{\rho C_p}, \tag{7}$$

$$\left(u\frac{\partial C}{\partial x} + v\frac{\partial C}{\partial y} + w\frac{\partial C}{\partial z}\right) = D_{\text{hnf}}\left(\frac{\partial^2 C}{\partial z^2}\right) - Kc(C - C_\infty). \tag{8}$$

Here, Kr is chemical reaction rate, R_1 and R_2 are the slip terms, Q_0 is the heat source term, k^* is the porosity term, $M_e(x) = xM_0$ and $M_e(y) = yM_0$ show the magnetic strength in x, y direction, and $F = xC_b/rk^{*1/2}$ is the nonuniform inertia factor constant.

Here Equation (1) describes the conservation of mass. Equation (2) shows the magnetic flux. Equations (3) and (4) are the momentum equations that pronounce the conduct of fluid flow. Equations (5) and (6) represent magnetic induction. Equations (7) and (8) are the energy and mass equations that describe the energy and mass transference around and near the wavy surface of the cylinder.

The initial and boundary conditions are as follows:

$$u = u_w + \mu_{\text{hnf}}R_1\frac{\partial u}{\partial z}, v = v_w + \mu_{\text{hnf}}R_1\frac{\partial v}{\partial z}, w = 0, M_1 = M_2 = M_3 = 0, T = T_w + k_{\text{hnf}}R_2\frac{\partial T}{\partial z}, C = C_0 \text{ at } z = 0$$
$$u \longrightarrow u_e, v \longrightarrow v_e, M_1 \longrightarrow M_e(x), M_2 \longrightarrow M_e(y), T \longrightarrow T_\infty, C \longrightarrow C_\infty \text{ at } z \longrightarrow \infty. \tag{9}$$

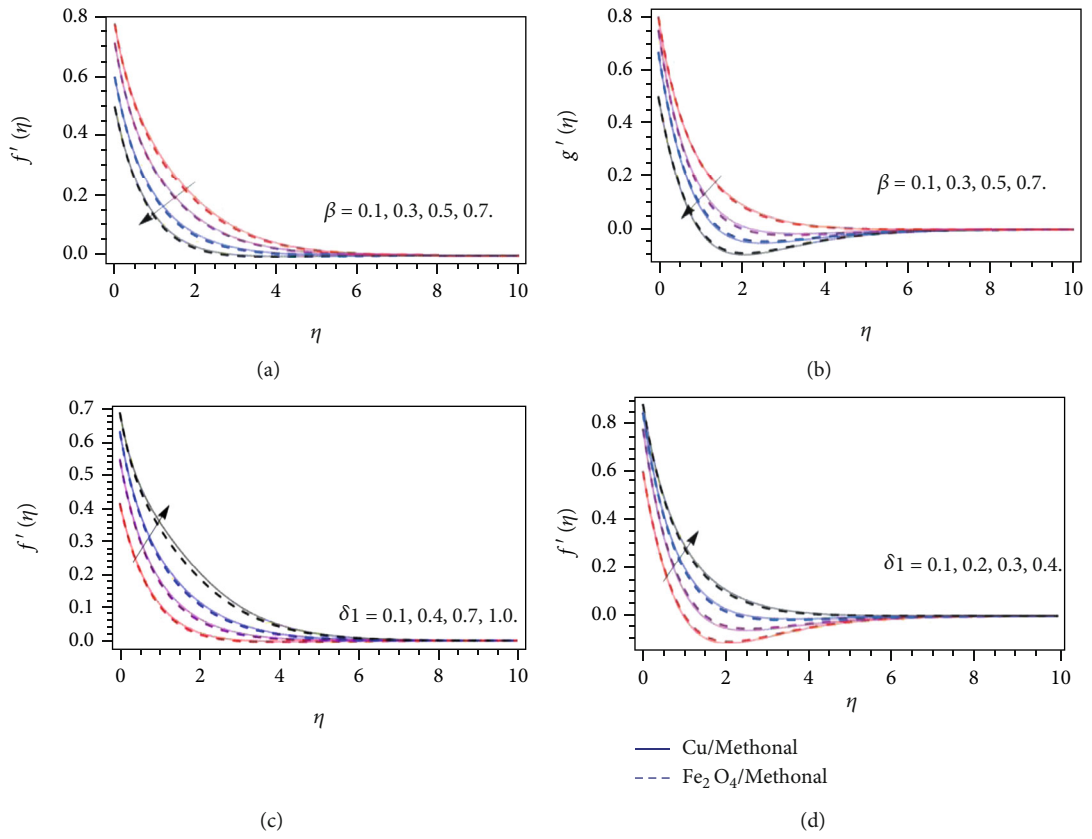

Figure 2: The presentation of velocity $(f(\eta), g(\eta))$ profile versus (a, b) magnetic parameter β and (c, d) velocity slip parameter δ_1.

The transformation variables are as follows:

$$u = axf'(\eta), v = byg'(\eta), w + (f(\eta) + cg(\eta))\sqrt{av} = 0,$$
$$M_1 = xM_0h_1(\eta) = 0, M_2 = yM_0h_2(\eta) = 0,$$
$$M_3 + \left(\frac{\nu_f}{a}\right)^{1/2}(h_1 + h_2)M_0 = 0, \eta = \sqrt{\frac{a}{\nu_f}}z, T = T_\infty + (T_w - T_\infty)\Theta(\eta), C = C_\infty + (C_w - C_\infty)\Phi(\eta) \tag{10}$$

By incorporating Equation (10), we get the following:

$$\frac{\hbar_1}{\hbar_2}(1 + cg + f)f'' - \frac{\beta}{\hbar_2}\left(h_1h''^2_1 + h_2h''_1 + 1\right) + 1 - Frf'^2 = 0, \tag{11}$$

$$\frac{\hbar_1}{\hbar_2}(1 + cg + f)g'' - \frac{\beta}{\hbar_2}\left(h_2h''^2_2 + h_1h_2 + 1\right) + c - Frcg'^2 = 0, \tag{12}$$

$$h''_1 + \left(h'_1f - f''h_1 - f''h_2 + ch'_1g\right)M = 0, \tag{13}$$

$$h''_2 + \left(h'_2f - cg''h_1 - cg''h_2 + ch'_2g\right)M = 0, \tag{14}$$

$$\frac{\hbar_4}{\hbar_3}\Theta''(\eta) + \Theta'(\eta) + c\Theta'(\eta)g + Q_0\Theta(\eta) = 0, \tag{15}$$

$$\hbar_6\varphi''(\eta) + \varphi'(\eta) + c\varphi'(\eta)g + Kr\varphi(\eta) = 0. \tag{16}$$

The transform conditions are as follows:

$$\left.\begin{array}{l} f(0) = 0, f'(0) = \delta_1\hbar_1 f''(\eta)_{\eta=0}, g(0) = 0, g'(0) = \hbar_1\delta_1 g''(\eta)_{\eta=0}, h_1(0) = 0, h_2(0) = 0 \\ \Theta(0) = \delta_2\hbar_4, \Phi(0) = 1 \text{ at } \eta = 0 \\ f'(\eta) \longrightarrow 0, g'(\eta) \longrightarrow 0, h_1(\eta) \longrightarrow 1, h_2(\eta) \longrightarrow 1, \Theta(\eta) \longrightarrow 0, \Phi(\eta) \longrightarrow 0 \text{ as } \eta = \infty \end{array}\right\}. \tag{17}$$

Here, $\hbar_1 = \mu_{\text{hnf}}/\mu_{bf}, \hbar_2 = \rho_{\text{hnf}}/\rho_{bf}, \hbar_3 = (\rho C_p)_{\text{hnf}}/(\rho C_p)_{bf}$, $\hbar_4 = k_{\text{hnf}}/k_{bf}, \hbar_5 = \sigma_{\text{hnf}}/\sigma_{bf}, \hbar_6 = D_{\text{hnf}}/D_{bf}$.

Here, h_1 and h_2 are magnetic field dimensionless terms. δ_1 and δ_2 are the velocity and thermal slip coefficient, where β is the magnetic parameters, Kr is the chemical reaction term, λ is the porosity term, Fr is the Forchheimer number, and Q_1 is the heat absorption and generation term defined as follows:

$$\beta = \frac{\mu_e}{4\pi\rho_f}\left(\frac{M_0}{a}\right)^2, M = \frac{\nu_f}{\eta_0}, Kr = \frac{K_c(1 - \lambda t)}{c}, \lambda = \frac{\nu}{k^*\Omega}, Fr = \frac{C_b}{k^{*1/2}}, Q_1 = \frac{xQ_0}{\rho C_p}. \tag{18}$$

Here, μ_e and η_0 are the magnetic absorptivity and diffusivity.

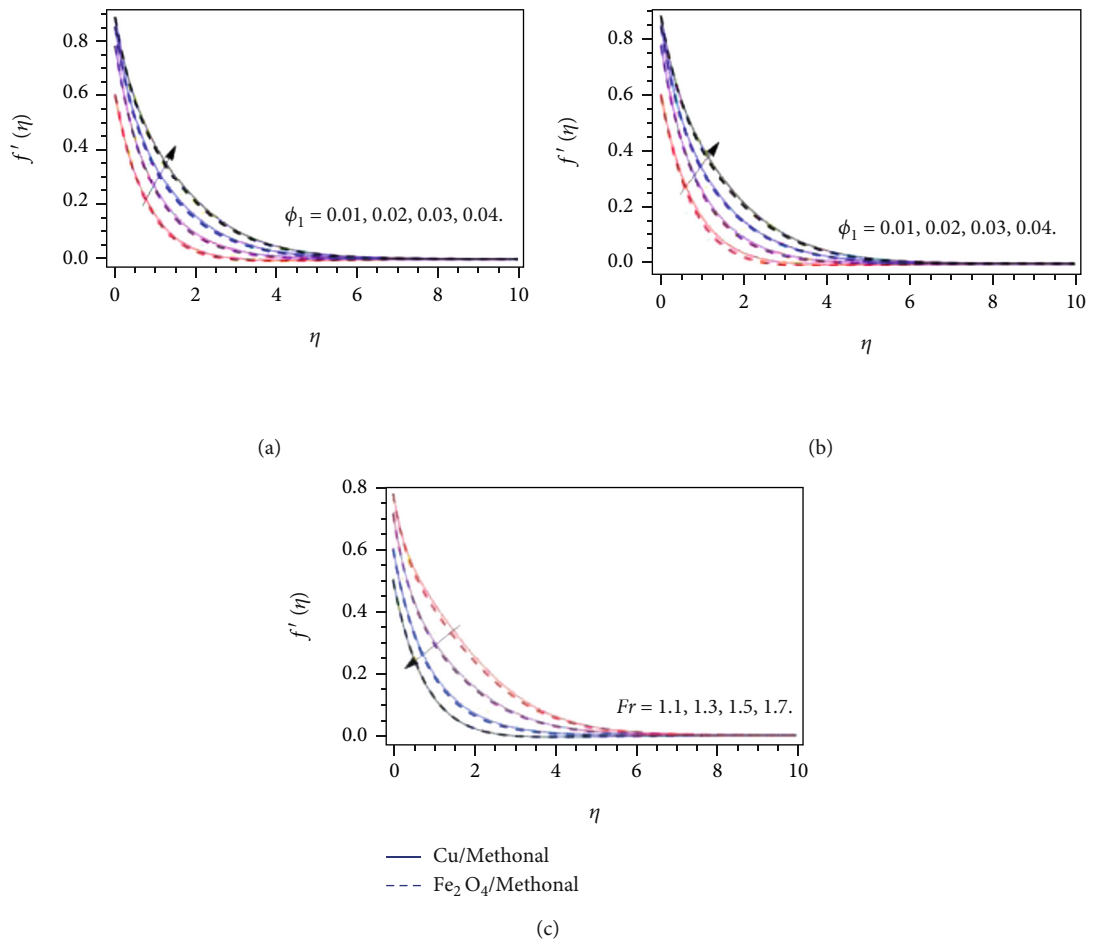

Figure 3: The performance of velocity $f(\eta)$ profile versus (a) copper ϕ_1 nanoparticles, (b) cobalt ferrite ϕ_2 nanoparticles, and (c) Darcy Forchheimer Fr.

The interest physical quantities are as follows:

$$C_{f_x} = \frac{\tau_{wx}|_{z=0}}{u_w^2 \rho_f}, C_{f_y} = \frac{\tau_{wy}|_{z=0}}{v_w^2 \rho_f}, Nu = \frac{q_w x}{(T_w - T_\infty)k_f}, Sh = \frac{j_w x}{(C_w - C_\infty)D_f}, \tag{19}$$

where

$$\begin{aligned} \tau_{wx} &= \mu_{\text{hnf}} \left(\frac{\partial u}{\partial z}\right)_{z=0}, \tau_{wy} = \mu_{\text{hnf}} \left(\frac{\partial v}{\partial z}\right)_{z=0}, \\ q_w &= -k_{\text{hnf}} \left(\frac{dT}{dz}\right)_{z=0}, j_w = -D_{\text{hnf}} \left(\frac{dC}{dz}\right)_{z=0}. \end{aligned} \tag{20}$$

The dimensionless form of Equation (19) is as follows:

$$\begin{aligned} \text{Re}^{1/2} C_{fx} &= \frac{cy}{x\hbar_1} f''(0), C_{fy} = \frac{cy}{x\hbar_1} g''(0), \text{Re}^{1/2} Nu_x \\ &= -\frac{k_{\text{hnf}}}{k_f} \Theta'(0), \text{Re}^{-1/2} Sh = -\Phi'(0). \end{aligned} \tag{21}$$

3. Numerical Solution

The main phases, while employing the parametric methodology, are as follows [34–38]:

Step 1. Simplifying the modeled equations

$$\left.\begin{aligned} &\vartheta_1 = f(\eta), \vartheta_2 = f'(\eta), \vartheta_3 = g(\eta), \vartheta_4 = g'(\eta), \vartheta_5 = h_1(\eta), \vartheta_6 = h_1'(\eta), \\ &\vartheta_7 = h_2(\eta), \vartheta_8 = h_2'(\eta), \vartheta_9(\eta) = \Theta(\eta), \vartheta_{10} = \Theta'(\eta), \vartheta_{11} = \Phi(\eta), \vartheta_{12} = \Phi'(\eta) \end{aligned}\right\}. \tag{22}$$

By putting (22) in (11)–(16) and (17), we get the following:

$$\frac{\hbar_1}{\hbar_2}(1 + c\vartheta_3 + \vartheta_1)\vartheta_2' - \frac{\beta}{\hbar_2}\left(\vartheta_5 {\vartheta'}^2{}_6 + \vartheta_7 \vartheta_1' + 1\right) + 1 - Fr\vartheta_2{}^2 = 0, \tag{23}$$

$$\frac{\hbar_1}{\hbar_2}(1 + c\vartheta_3 + \vartheta_1)\vartheta_4' - \frac{\beta}{\hbar_2}\left(\vartheta_7 {\vartheta'}^2{}_8 + \vartheta_5 \vartheta_7 + 1\right) + c - Frc\vartheta_4{}^2 = 0, \tag{24}$$

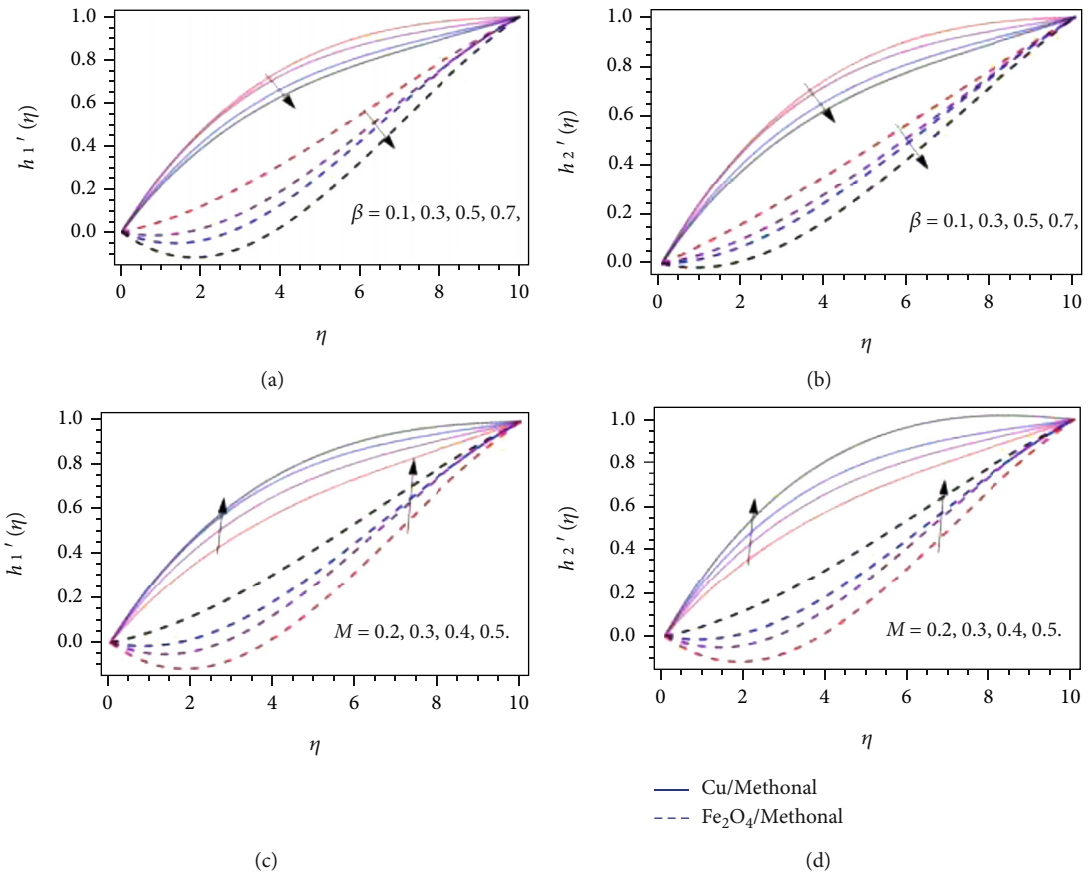

Figure 4: The performance of induced magnetic field $(h_1'(\eta), h_2'(\eta))$ profile versus (a, b) magnetic parameter β and (c, d) magnetic Prandtl number M.

$$\vartheta_6' + \left(\vartheta_6\vartheta_1 - \vartheta_2'\vartheta_5 - \vartheta_2'\vartheta_7 + c\vartheta_6\vartheta_3\right)M = 0, \tag{25}$$

$$\vartheta_8' + \left(\vartheta_8\vartheta_1 - c\vartheta_4'\vartheta_5 - c\vartheta_4'\vartheta_7 + ch\vartheta_8\vartheta_3\right)M = 0, \tag{26}$$

$$\frac{\hbar_4}{\hbar_3}\vartheta_{10}'(\eta) + \vartheta_{10}(\eta) + c\vartheta_{10}(\eta)g + Q_0\vartheta_9(\eta) = 0, \tag{27}$$

$$\hbar_6\vartheta_{12}'(\eta) + \vartheta_{12}(\eta) + c\vartheta_{12}(\eta)\vartheta_3 + Kr\vartheta_{11}(\eta) = 0, \tag{28}$$

and the transform conditions are as follows:

$$\left.\begin{aligned}&\vartheta_1(0) = 0, \vartheta_2(0) = \delta_1\hbar_1\vartheta_2'(\eta)_{\eta=0}, \vartheta_3(0) = 0, \vartheta_4(0) = \delta_1\hbar_1\vartheta_4'(\eta)_{\eta=0}, \vartheta_5(0) = 0, \vartheta_7(0) = 0,\\&\vartheta_9(0) = \delta_2\hbar_4, \vartheta_{11}(0) = 1 \text{ at } \eta = 0,\\&\vartheta_2(\eta) \longrightarrow 0, \vartheta_4(\eta) \longrightarrow 0, \vartheta_5(\eta) \longrightarrow 1, \vartheta_7(\eta) \longrightarrow 1, \vartheta_9(\eta) \longrightarrow 0, \vartheta_{11}(\eta) \longrightarrow 0 \text{ as } \eta = \infty\end{aligned}\right\}. \tag{29}$$

Step 2. Introducing parameter p

$$\frac{\hbar_1}{\hbar_2}(1 + c\vartheta_3 + \vartheta_1)\vartheta_2' - \frac{\beta}{\hbar_2}\left(\vartheta_5\vartheta'^2{}_6 + \vartheta_7\vartheta_1' + 1\right) + 1 - Fr\left(\vartheta_2{}^2 - 1\right)p = 0, \tag{30}$$

$$\vartheta_6' + \left(\vartheta_1(\vartheta_6 = 1)p - \vartheta_2'\vartheta_5 - \vartheta_2'\vartheta_7 + c\vartheta_6\vartheta_3\right)M = 0, \tag{31}$$

$$\vartheta_8' + \left(\vartheta_1(\vartheta_8 - 1)p - c\vartheta_4'\vartheta_5 - c\vartheta_4'\vartheta_7 + ch\vartheta_8\vartheta_3\right)M = 0, \tag{32}$$

$$\frac{\hbar_4}{\hbar_3}\vartheta_{10}'(\eta) + (\vartheta_{10}(\eta) -)p + c\vartheta_{10}(\eta)g + Q_0\vartheta_9(\eta) = 0, \tag{33}$$

$$\hbar_6\vartheta_{12}'(\eta) + (\vartheta_{12}(\eta) - 1)p + c\vartheta_{12}(\eta)\vartheta_3 + Kr\vartheta_{11}(\eta) = 0. \tag{34}$$

Step 3. Differentiating by parameter "p"

By differentiating Equations (30)–(34) w. r. t parameter p , we get the following:

$$V' = AV + R, \tag{35}$$

$$\frac{d\zeta_i}{d\tau}, \tag{36}$$

where $i = 1, 2, \cdots\cdots\cdots 11$.

Step 4. Applying the superposition principle

$$V = aU + W. \tag{37}$$

For each element, resolve the two Cauchy problems listed below.

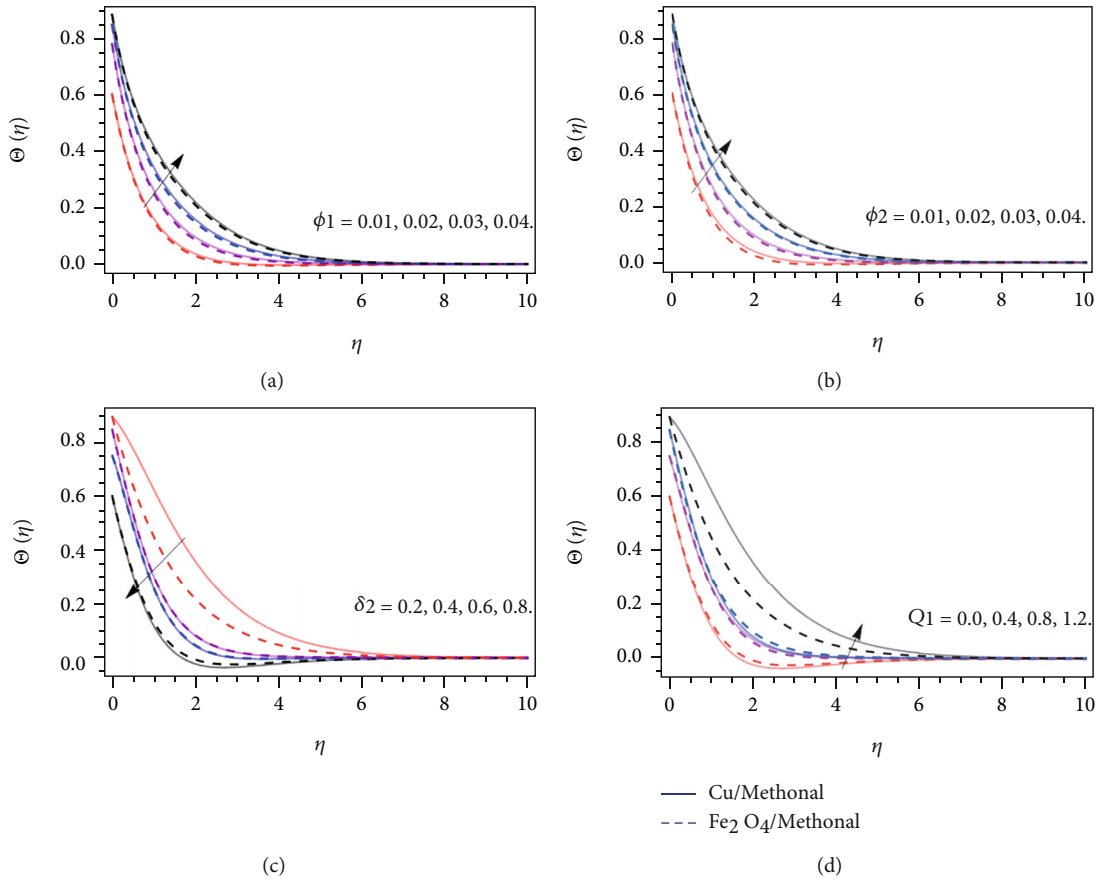

FIGURE 5: The performance of energy $\Theta(\eta)$ profile versus (a) copper ϕ_1 nanoparticles, (b) cobalt ferrite ϕ_2 nanoparticles, (c) thermal jump parameter δ_2, (d) heat source term Q_1.

$$U = aU, \tag{38}$$

$$W' = AW + R. \tag{39}$$

By putting Equation (39) in Equation (37), we get

$$(aU + W)' = A(aU + W) + R. \tag{40}$$

Step 5. Solving the Cauchy problems

By utilizing implicit scheme,

$$\frac{U^{i+1} - U^i}{\Delta\eta} = AU^{i+1}, \frac{W^{i+1} - W^i}{\Delta\eta} = AW^{i+1}. \tag{41}$$

The final iterative form is as follows:

$$U^{i+1} = \frac{U^i}{(I - \Delta\eta A)}, W^{i+1} = \frac{(W^i + \Delta\eta R)}{(I - \Delta\eta A)}. \tag{42}$$

4. Result and Discussion

The preceding is some of the findings that have been noticed:

Velocity profile $(f(\eta), g(\eta))$

Figures 2(a)–2(d) particularize the presentation of velocity $(f(\eta), g(\eta))$ profile against the variation of magnetic parameter β and velocity slip term δ_1, respectively. Figures 2(a) and 2(b) reveal that the fluid velocity profile reduces under the upshot of the magnetic term β. Physically, it is clear that the magnetic field creates resistive force around its self, which provides hurdles (Lorentz force) to the flow field, and as a result, fluid flow declines. Figures 2(c) and 2(d) show that the fluid velocity diminishes with the varying effect of velocity slip term δ_1.

Figures 3(a)–3(c) illustrate the performance of velocity $f(\eta)$ profile against the variation of copper ϕ_1 nanoparticles, cobalt ferrite ϕ_2 nanoparticles, and Darcy Forchheimer Fr, respectively. Figures 3(a) and 3(b) expose that the velocity field substantially boosts with the action of copper ϕ_1 and cobalt ferrite ϕ_2 nanoparticles. The specific heat capacity of methanol is remarkably greater, while the thermal conductivity is less than the copper and cobalt ferrite nanomaterials, that is why the inclusion of hybrid nanoparticles, especially copper, reduces its average heat-absorbing efficiency, which results in the enhancement of velocity field. The upshot of Darcy Forchheimer's number degenerates the velocity distribution as shown in Figure 3(c).

Induced magnetic field $(h_1'(\eta), h_2'(\eta))$

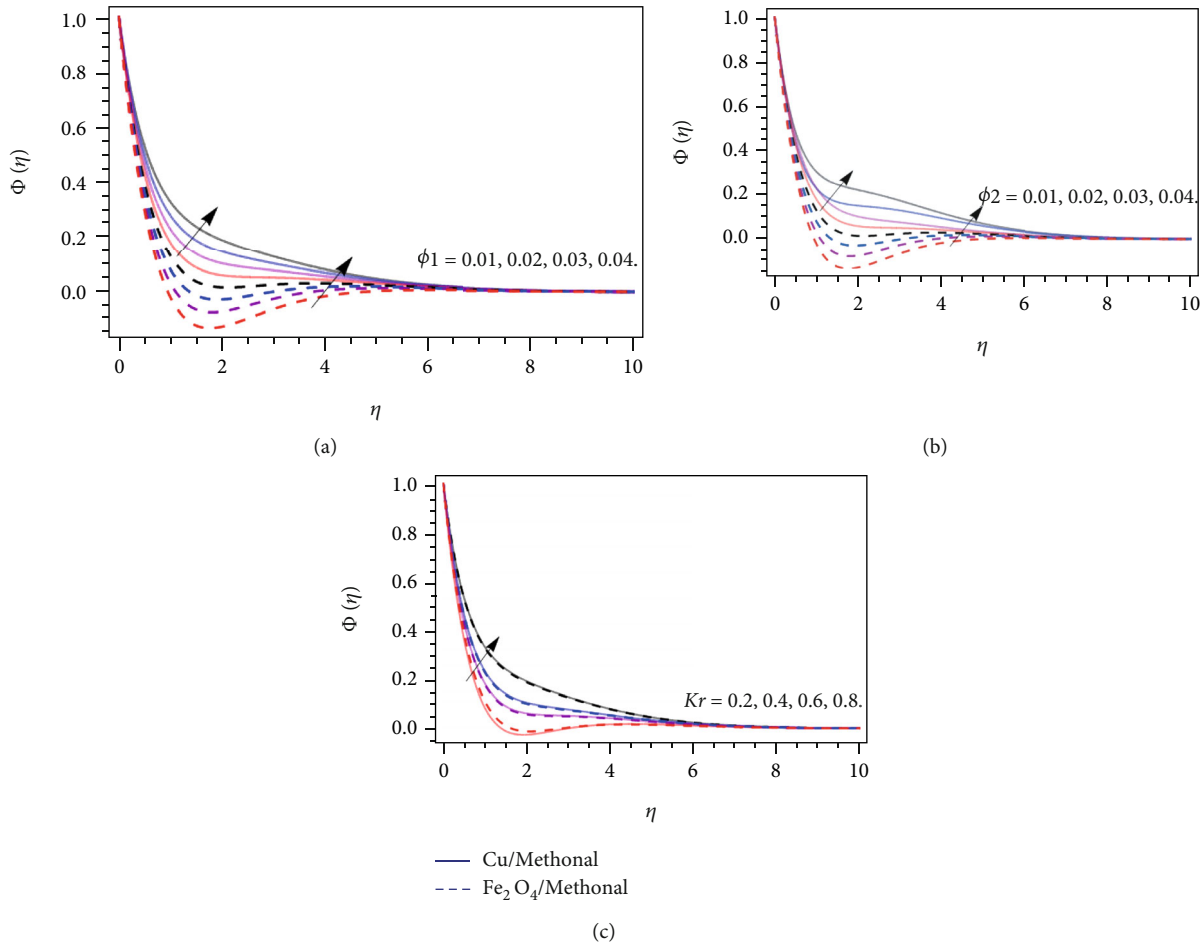

Figure 6: The performance of concentration $\Phi(\eta)$ profile versus (a) copper ϕ_1 nanoparticles, (b) cobalt ferrite ϕ_2 nanoparticles, and (c) chemical reaction term Kr.

Table 1: The statistical properties of copper, cobalt iron oxide, and methanol [32, 33].

	ρ (kg/m^3)	C_p (j/kgK)	k (W/mK)	σ (S/m)
Methanol	792	2545	0.2035	0.5×10^{-6}
Copper (Cu)	8933	385	401	5.96×10^{7}
$CoFe_2O_4$	4907	700	3.7	5.51×10^{9}

Figures 4(a)–4(d) highlight the presentation of $(h_1'(\eta), h_2'(\eta))$ profiles versus β (magnetic constraint) and M. Figures 4(a) and 4(b) show that the induced magnetic field profile decreases with the effect of the magnetic parameter β. Actually, the improving values of magnetic term suppressed the induced magnetic field which indicates deteriorating conduct of the induced magnetic field. Figures 4(c) and 4(d) report that the positive influence of M encourages the $(h_1'(\eta), h_2'(\eta))$ profiles. The fundamental reason for this is that multiplying the ratios of M corresponds to a reduced magnetic diffusive, resulting in a loss of magnetic field strength. It improves the curve. Hence, the rising credit of M improves the induced magnetic field profile.

Temperature profile $\Theta(\eta)$

Figures 5(a)–5(d) illustrate the performance of energy $\Theta(\eta)$ profile against the variation of copper ϕ_1 nanoparticles, cobalt ferrite ϕ_2 nanoparticles, thermal jump parameter δ_2, and heat source term Q_1. Figures 5(a) and 5(b) explain that the energy $\Theta(\eta)$ profile boosts with the positive variation of copper ϕ_1 and cobalt ferrite ϕ_2 nanoparticles. We have discussed before that the thermal conductivity of fluid enhances, while specific heat capacity is condensed under the action of copper ϕ_1 and cobalt ferrite ϕ_2 nanoparticles. That is why such a situation has been noticed in Figures 5 (a) and 5(b). Figures 5(c) and 5(d) show an opposite behavior of energy profile versus thermal jump parameter δ_2 and heat source term Q_1. The energy profile declines due to the variation of thermal jump constraint. To put it another way, the energy field is a diminishing function δ_2. Logically, increasing δ_2 enables the wavy cylinder to expand. As a result of this, the thickness of the cylinder rises, reducing the energy field curvature. Heat is emitted as energy by nanosized particles in practice. The more the input of microparticles, the greater the heat production as energy. The heat absorption and generation term Q_1 boost the temperature field because its effect generates heat, which causes the rises in energy profile as shown in Figure 5(d).

Table 2: The thermal properties of the hybrid nanofluid ($\phi_1 = \phi_{Cu}, \phi_2 = \phi_{CoFe_2O_4}$) [32, 33].

Properties	
Viscosity	$\mu_{hnf}/\mu_{bf} = 1/(1-\phi_{Cu}-\phi_{CoFe_2O_4})^2$
Density	$\rho_{hnf}/\rho_{bf} = \phi_{Cu}(\rho_{Cu}/\rho_{bf}) + \phi_{CoFe_2O_4}\left(\rho_{CoFe_2O_4}/\rho_{bf}\right) + (1-\phi_{Cu}-\phi_{CoFe_2O_4})$
Thermal capacity	$(\rho C_p)_{hnf}/(\rho C_p)_{bf} = \phi_{Cu}((\rho C_p)_{Cu}/(\rho C_p)_{bf}) + \phi_{CoFe_2O_4}\left((\rho C_p)_{CoFe_2O_4}/(\rho C_p)_{bf}\right) + (1-\phi_{Cu}-\phi_{CoFe_2O_4})$
Thermal conductivity	$k_{hnf}/k_{bf} = [(\phi_{Cu}k_{Cu} + \phi_{CoFe_2O_4}k_{CoFe_2O_4}/\phi_{Cu} + \phi_{CoFe_2O_4}) + 2k_{bf} + 2(\phi_{Cu}k_{Cu} + \phi_{CoFe_2O_4}k_{CoFe_2O_4}) - 2(\phi_{Cu} + \phi_{CoFe_2O_4})k_{bf}/\left(\phi_{Cu}k_{Cu} + \phi_{CoFe_2O_4}k_{CoFe_2O_4}/\phi_{Cu} + \phi_{CoFe_2O_4}\right) + 2k_{bf} - 2(k_{Cu}\phi_{Cu} + k_{CoFe_2O_4}\phi_{CoFe_2O_4}) + (\phi_{Cu} + \phi_{CoFe_2O_4})2k_{bf}]$
Electrical conductivity	$\sigma_{hnf}/\sigma_{bf} = [(\phi_{Cu}\sigma_{Cu} + \sigma_{CoFe_2O_4}\phi_{CoFe_2O_4}/\phi_{CoFe_2O_4} + \phi_{Cu}) + 2\sigma_{bf} + 2(\phi_{Cu}\sigma_{Cu} + \phi_{CoFe_2O_4}\sigma_{CoFe_2O_4}) - 2\left(\phi_{Cu} + \phi_{CoFe_2O_4}\right)\sigma_{bf}/\left(\phi_{Cu}\sigma_{Cu} + \phi_{CoFe_2O_4}\sigma_{CoFe_2O_4}/\phi_{Cu} + \phi_{CoFe_2O_4}\right) + 2\sigma_{bf} - (\phi_{Cu}\sigma_{Cu} + \phi_{CoFe_2O_4}\sigma_{CoFe_2O_4}) + (\phi_{Cu} + \phi_{CoFe_2O_4})\sigma_{bf}]$

Table 3: Statistical results for Nusselt number.

δ_2	Q_1	ϕ_1, ϕ_2	PCM $(k_{nf}/k_f)\,\Theta'(0)$	bvp4c $(k_{nf}/k_f)\,\Theta'(0)$	PCM $(k_{hnf}/k_f)\,\Theta'(0)$	bvp4c $(k_{hnf}/k_f)\Theta'(0)$
0.2			0.0475535	0.0474435	0.0484531	0.0484431
0.4			0.0355123	0.0354042	0.0366122	0.0366023
0.6			0.0365852	0.0364743	0.0369853	0.0369752
0.8			0.0292107	0.0291003	0.0271407	0.0271323
	0.0		0.0565588	0.0564476	0.0554555	0.0554456
	0.4		0.0575760	0.0574652	0.0575961	0.0575854
	0.8		0.0579962	0.0578861	0.0589965	0.0589846
	1.2	0.01	0.0674420	0.06734310	0.0683460	0.0683350
		0.02	0.0684241	0.0683220	0.0693271	0.0693160
		0.03	0.0691324	0.0690313	0.0713142	0.0713041
		0.04	0.0722419	0.0723407	0.0743319	0.0743217

Table 4: Numerical outcomes for Sherwood number.

Kr	ϕ_1, ϕ_2	PCM $(D_{nf}/D_f)\Phi'(0)$	bvp4c $(D_{nf}/D_f)\Phi'(0)$	PCM $\left(D_{hnf}/D_f\right)\Phi'(0)$	bvp4c $\left(D_{hnf}/D_f\right)\Phi'(0)$
0.2		0.0632428	0.0632228	0.0642421	0.0642220
0.4		0.0629422	0.0629210	0.0639437	0.0639234
0.6		0.0615944	0.0615742	0.0614946	0.0614743
0.8		0.5930362	0.5930160	0.5910341	0.5910141
	0.01	0.0627713	0.0627511	0.0677736	0.0677634
	0.02	0.0638833	0.0638631	0.0728855	0.0728651
	0.03	0.6687551	0.6687340	0.7774605	0.7774402
	0.04	0.7026619	0.7026617	0.7906815	0.7906613

Concentration profile $\Phi(\eta)$

Figures 6(a)–6(c) report the performance of concentration $\Phi(\eta)$ profile versus copper ϕ_1 nanoparticles, cobalt ferrite ϕ_2 nanoparticles, and chemical reaction term Kr, respectively. Figures 6(a) and 6(b) describe that the mass transfer $\Phi(\eta)$ profile improves with the positive deviation of copper ϕ_1 and cobalt ferrite ϕ_2 nanoparticulate. We have reviewed earlier that the thermal conductivity of fluid enhances, while specific heat capacity is condensed under the action of copper ϕ_1 and cobalt ferrite ϕ_2 nanoparticles. That is why such a situation has been noticed in Figures 6(a) and 6(b). The chemical reaction coefficient positively affects the mass transfer, because it also encourages fluid particles to move fast, which results in the positive variation as elaborated in Figure 6(c).

Tables 1 and 2 exemplify the thermochemical possessions and model of base fluid, copper, and cobalt iron oxide

individually. Tables 3 and 4 report the statistical assessment of PCM and bvp4c techniques, to confirm the legality of the current report. The energy field and mass transition profile are associated with the determination. Tables 3 and 4 also reveal the comparative assessments between simple and hybrid NF. It has been clearly perceived that the mass and heat transfer ratio of hybrid NF as compared to simple NF or ordinary fluid is greater.

5. Conclusion

The objective of this research is to build a computational model to investigate the effects of methanol-based hybrid NFs consisting of Cu and $CoFe_2O_4$ nanoparticles on heat and mass communication. The fluid flow has been examined in a heated wavy flexible cylinder under the impact of slip condition, variable thickness, Darcy Forchheimer, heat absorption/generation, and chemical reaction. The PCM approach is used to simulate the problem, and the results are compared to those obtained using the Matlab software bvp4c. The key observations are as follows:

(i) The velocity profile reduces with the effect of the magnetic parameter β, velocity slip constant δ_1, and Darcy Forchheimer's number Fr

(ii) The velocity and energy field significantly boosts with the inclusion of copper ϕ_1 and cobalt ferrite ϕ_2 nanoparticulates in the base fluid methanol

(iii) The $(h_1'(\eta), h_2'(\eta))$ profile decreases with the effect of the β, while enhances under the action of parameter M

(iv) The energy profile declines due to the variation of thermal jump constraint and boosts with the absorption and generation term Q_1

(v) The mass propagation rate can be significantly enhancing with the effect of chemical reaction parameter Kr

(vi) The hybrid NF has greater tendency to enhance the energy and velocity of base fluid as compared to the ordinary NF

Data Availability

No data were used to support this study.

Conflicts of Interest

The authors have declared no conflict of interest.

Acknowledgments

The authors are thankful to the Deanship of Scientific Research, King Khalid University, Abha, Saudi Arabia, for financially supporting this work through the General Research Project under Grant no. R.G.P.2/160/43. Taif University Researchers Supporting Project number (TURSP-2020/31), Taif University, Taif, Saudi Arabia.

References

[1] S. H. Nam and H. S. Yoon, "Effect of the wavy geometric disturbance on the flow over elliptic cylinders with different aspect ratios," *Ocean Engineering*, vol. 243, p. 110287, 2022.

[2] K. Cavanagh and R. Wulandana, "2D flow past a confined circular cylinder with sinusoidal ridges," 2019.

[3] T. Salahuddin, A. M. Bashir, M. Khan, and W. F. Xia, "Multiple shaped nano-particles influence on thermal conductivity of fluid flow between inflexible and sinusoidal walls," *Case studies in thermal engineering*, vol. 25, p. 100930, 2021.

[4] B. Wu, S. Li, L. Zhang, and K. Li, "Experimental determination of the two-dimensional aerodynamic admittances of a 5: 1 rectangular cylinder in streamwise sinusoidal flows," *Journal of Wind Engineering and Industrial Aerodynamics*, vol. 210, p. 104525, 2021.

[5] M. Bilal, A. Saeed, M. M. Selim, T. Gul, I. Ali, and P. Kumam, "Comparative numerical analysis of Maxwell's time-dependent thermo-diffusive flow through a stretching cylinder," *Case Studies in Thermal Engineering*, vol. 27, p. 101301, 2021.

[6] Y. M. Seo, K. Luo, M. Y. Ha, and Y. G. Park, "Direct numerical simulation and artificial neural network modeling of heat transfer characteristics on natural convection with a sinusoidal cylinder in a long rectangular enclosure," *International Journal of Heat and Mass Transfer*, vol. 152, p. 119564, 2020.

[7] M. Bilal, I. Khan, T. Gul et al., "Darcy-forchheimer hybrid nano fluid flow with mixed convection past an inclined cylinder," *CMC-Computers Materials & Continua*, vol. 66, no. 2, pp. 2025–2039, 2021.

[8] A. Sarchami, M. Najafi, A. Imam, and E. Houshfar, "Experimental study of thermal management system for cylindrical Li-ion battery pack based on nanofluid cooling and copper sheath," *International Journal of Thermal Sciences*, vol. 171, p. 107244, 2022.

[9] I. Ullah, T. Hayat, A. Alsaedi, and S. Asghar, "Dissipative flow of hybrid nanoliquid (H2O-aluminum alloy nanoparticles) with thermal radiation," *Physica Scripta*, vol. 94, no. 12, p. 125708, 2019.

[10] M. Shuaib, A. Ali, M. A. Khan, and A. Ali, "Numerical investigation of an unsteady nanofluid flow with magnetic and suction effects to the moving upper plate," *Advances in Mechanical Engineering*, vol. 12, no. 2, 2020.

[11] H. Waqas, M. Imran, T. Muhammad, S. M. Sait, and R. Ellahi, "Numerical investigation on bioconvection flow of Oldroyd-B nanofluid with nonlinear thermal radiation and motile microorganisms over rotating disk," *Journal of Thermal Analysis & Calorimetry*, vol. 145, no. 2, pp. 523–539, 2021.

[12] B. Mussabayeva, K. Murzagulova, Z. Aripzhanova, and A. Klivenko, "Preparation of silver and copper nanoparticles for biomedical application," in *2017 IEEE 7th International Conference Nanomaterials: Application & Properties*, Zatoka, Ukraine, Sep 2017.

[13] H. H. Kart, H. Yildirim, S. O. Kart, and T. Çağin, "Physical properties of Cu nanoparticles: a molecular dynamics study," *Materials Chemistry and Physics*, vol. 147, no. 1-2, pp. 204–212, 2014.

[14] S. Munjal, N. Khare, C. Nehate, and V. Koul, "Water dispersible CoFe2O4 nanoparticles with improved colloidal stability for biomedical applications," *Journal of Magnetism and Magnetic Materials*, vol. 404, pp. 166–169, 2016.

[15] V. Nica, C. Caro, J. M. Páez-Muñoz, M. P. Leal, and M. L. Garcia-Martin, "Bi-magnetic core-shell CoFe2O4@ MnFe2O4 nanoparticles for in vivo theranostics," *Nanomaterials*, vol. 10, no. 5, p. 907, 2020.

[16] M. Bilal, T. Gul, A. Alsubie, and I. Ali, "Axisymmetric hybrid nanofluid flow with heat and mass transfer amongst the two gyrating plates," *ZAMM-Journal of Applied Mathematics and Mechanics/Zeitschrift für Angewandte Mathematik und Mechanik*, vol. 101, no. 11, article e202000146, 2021.

[17] G. K. Ramesh, J. K. Madhukesh, B. C. Prasannakumara, S. A. Shehzad, and F. M. Abbasi, "Thermodynamics examination of Fe3O4-CoFe2O4/water+ EG nanofluid in a heated plate: crosswise and stream-wise aspects," *Arabian Journal for Science and Engineering*, pp. 1–10, 2021.

[18] J. Wang, Y. P. Xu, R. Qahiti et al., "Simulation of hybrid nanofluid flow within a microchannel heat sink considering porous media analyzing CPU stability," *Journal of Petroleum Science and Engineering*, vol. 208, p. 109734, 2022.

[19] M. Ibrahim, A. Abidi, E. A. Algehyne, T. Saeed, G. Cheraghian, and M. Sharifpur, "Improvement of the energy and exergy efficiencies of the parabolic solar collector equipped with a twisted turbulator using SWCNT-Cu/water two-phase hybrid nanofluid," *Sustainable Energy Technologies and Assessments*, vol. 49, p. 101705, 2022.

[20] M. Yaseen, S. K. Rawat, and M. Kumar, "Hybrid nanofluid (MoS2–SiO2/water) flow with viscous dissipation and Ohmic heating on an irregular variably thick convex/concave-shaped sheet in a porous medium," *Heat Transfer*, vol. 51, no. 1, pp. 789–817, 2022.

[21] F. Wang, Z. Xiao, X. Liu et al., "Strategic design of cellulose nanofibers@ zeolitic imidazolate frameworks derived mesoporous carbon-supported nanoscale CoFe2O4/CoFe hybrid composition as trifunctional electrocatalyst for Zn-air battery and self-powered overall water-splitting," *Journal of Power Sources*, vol. 521, p. 230925, 2022.

[22] I. Ullah, R. Ali, I. Khan, and K. S. Nisar, "Insight into kerosene conveying CNTs and Fe3O4 nanoparticles through a porous medium: significance of Coriolis force and entropy generation," *Physica Scripta*, vol. 96, no. 5, article 055705, 2021.

[23] I. Ullah, T. Hayat, A. Alsaedi, and H. M. Fardoun, "Numerical treatment of melting heat transfer and entropy generation in stagnation point flow of hybrid nanomaterials (SWCNT-MWCNT/engine oil)," *Modern Physics Letters B*, vol. 35, no. 6, p. 2150102, 2021.

[24] T. Hayat, I. Ullah, T. Muhammad, and A. Alsaedi, "Hydromagnetic squeezed flow of second-grade nanomaterials between two parallel disks," *Journal of Thermal Analysis and Calorimetry*, vol. 139, no. 3, pp. 2067–2077, 2020.

[25] I. Ullah, T. Hayat, and A. Alsaedi, "Nonlinear radiative squeezed flow of nanofluid subject to chemical reaction and activation energy," *Journal of Heat Transfer*, vol. 142, no. 8, 2020.

[26] T. Hayat and S. Noreen, "Peristaltic transport of fourth grade fluid with heat transfer and induced magnetic field," *Comptes Rendus Mécanique*, vol. 338, no. 9, pp. 518–528, 2010.

[27] M. C. Raju, S. V. K. Varma, and B. Seshaiah, "Heat transfer effects on a viscous dissipative fluid flow past a vertical plate in the presence of induced magnetic field," *Ain Shams Engineering Journal*, vol. 6, no. 1, pp. 333–339, 2015.

[28] N. S. Khashi'ie, N. M. Arifin, and I. Pop, "Magnetohydrodynamics (MHD) boundary layer flow of hybrid nanofluid over a moving plate with Joule heating," *Alexandria Engineering Journal*, vol. 61, no. 3, pp. 1938–1945, 2022.

[29] M. Khazayinejad and S. S. Nourazar, "On the effect of spatial fractional heat conduction in MHD boundary layer flow using Gr-Fe3O4–H2O hybrid nanofluid," *International Journal of Thermal Sciences*, vol. 172, p. 107265, 2022.

[30] I. Ullah, "Activation energy with exothermic/endothermic reaction and Coriolis force effects on magnetized nanomaterials flow through Darcy–Forchheimer porous space with variable features," *Waves in Random and Complex Media*, pp. 1–14, 2022.

[31] T. Salahuddin, N. Siddique, M. Khan, and Y. M. Chu, "A hybrid nanofluid flow near a highly magnetized heated wavy cylinder," *Alexandria Engineering Journal*, vol. 61, no. 2, pp. 1297–1308, 2022.

[32] P. B. A. Reddy, "Biomedical aspects of entropy generation on electromagnetohydrodynamic blood flow of hybrid nanofluid with nonlinear thermal radiation and non-uniform heat source/sink," *The European Physical Journal Plus*, vol. 135, no. 10, pp. 1–30, 2020.

[33] C. Sulochana, S. R. Aparna, and N. Sandeep, "Impact of linear/nonlinear radiation on incessantly moving thin needle in MHD quiescent Al-Cu/methanol hybrid nanofluid," *International Journal of Ambient Energy*, pp. 1–7, 2020.

[34] M. Shuaib, R. A. Shah, I. Durrani, and M. Bilal, "Electrokinetic viscous rotating disk flow of Poisson-Nernst-Planck equation for ion transport," *Journal of Molecular Liquids*, vol. 313, p. 113412, 2020.

[35] M. Shuaib, R. A. Shah, and M. Bilal, "Von-Karman rotating flow in variable magnetic field with variable physical properties," *Advances in Mechanical Engineering*, vol. 13, no. 2, 2021.

[36] H. Alrabaiah, M. Bilal, M. A. Khan, T. Muhammad, and E. Y. Legas, "Parametric estimation of gyrotactic microorganism hybrid nanofluid flow between the conical gap of spinning disk-cone apparatus," *Scientific Reports*, vol. 12, no. 1, pp. 1–14, 2022.

[37] A. Ahmadian, M. Bilal, M. A. Khan, and M. I. Asjad, "Numerical analysis of thermal conductive hybrid nanofluid flow over the surface of a wavy spinning disk," *Scientific Reports*, vol. 10, no. 1, pp. 1–13, 2020.

[38] Y. P. Lv, E. A. Algehyne, M. G. Alshehri et al., "Numerical approach towards gyrotactic microorganisms hybrid nanoliquid flow with the hall current and magnetic field over a spinning disk," *Scientific Reports*, vol. 11, no. 1, pp. 1–13, 2021.